A robust asymmetric diatomic electrocatalyst for oxygen reduction reaction in both acidic and alkaline media

Pianpian Zhang [a], Tingting Sun [a,*], Rong Jiang [a], Tianyu Zheng [a], Qingmei Xu [a], Ruanbo Hu [b], Xinxin Wang [a], Kang Wang [a], Lianbin Xu [c], Dingsheng Wang [d], Jianzhuang Jiang [a]

[a] Beijing Advanced Innovation Center for Materials Genome Engineering, Beijing Key Laboratory for Science and Application of Functional Molecular and Crystalline Materials, Department of Chemistry and Chemical Engineering, School of Chemistry and Biological Engineering, University of Science and Technology Beijing, Beijing 100083, China
[b] State Key Lab of Organic-Inorganic Composites and Beijing Advanced Innovation Center for Soft Matter Science and Engineering, Beijing University of Chemical Technology, Beijing 100029, China
[c] State Key Laboratory of Organic-Inorganic Composites, Beijing University of Chemical Technology, Beijing 100029, China
[d] Department of Chemistry, Tsinghua University, Beijing 100084, China

ARTICLE INFO

ABSTRACT

Herein, an asymmetric diatomic site oxygen reduction reaction (ORR) electrocatalyst with atomically dispersed Fe and Cu species co-anchored on porous nitrogen-doped polyhedra carbon was successfully prepared through a facile cooperation of post-adsorption and two-step pyrolysis method. Density functional theory (DFT) calculations reveal that the asymmetric FeCu dual atomic site experiences a symmetry destruction of electron transfer due to the existing Cu-N_4 sites and thus results in the electron redistribution in $Fe_{SA}Cu_{SA}/NC$, contributing significantly to the optimization of intermediates adsorption and acceleration of kinetics during ORR process. Attributed to the structural advantages of Fe_{SA}-N_4&Cu_{SA}-N_4 sites and highly porous carbon matrix, the $Fe_{SA}Cu_{SA}/NC$ catalyst exhibits excellent electrocatalytic ORR performance with half-wave potentials ($E_{1/2}$) of 0.86 and 0.88 V versus reversible hydrogen electrode in 0.1 M $HClO_4$ and 0.1 M KOH solutions as well as high durability. Moreover, $Fe_{SA}Cu_{SA}/NC$-based H_2/O_2 fuel cell and zinc-air battery present superior performance with high peak power density.

1. Introduction

To alleviate the rapid increasing environmental pollution and energy demand, proton exchange membrane fuel cells (PEMFCs) and zinc–air batteries (ZABs) with high energy density and cleanness without greenhouse gas emission have been proposed as an advanced and renewable energy candidate to traditional fossil fuel technologies [1–6]. Generally speaking, in evaluating the overall efficiency of PEMFCs and ZABs, electrochemical oxygen reduction reaction (ORR) acts as a decisive role [7]. Up to now, electrocatalysts based on platinum-group metals have been widely employed as commercial benchmark catalysts to improve the multi-electron transfer ORR with dynamically sluggish kinetics at the cathode of PEMFCs and air electrode of ZABs, but the flaws of scarcity, unsatisfying stability, and prohibitive cost of platinum severely hinder the widespread implementation of PEMFCs and ZABs [8–11]. Eexploring high-efficiency and economical noble-metal free ORR catalysts to substitute platinum-group-based catalytic materials is therefore extremely demanded yet remains great challenging to realize the sustainability of industrial use of PEMFCs and ZABs [12–17].

Among a variety of noble-metal free catalysts, transition metal-nitrogen-carbon (M-N-C) catalysts containing single atomic M-N_x active sites have aroused significant attention as high-performance ORR catalysts thanks to their nearly 100% utilization of metal atoms, abundant resources, and tunable electronic configuration [18–22]. In particular, single atom Fe-N-C catalysts (Fe_{SA}-N-C) containing Fe-N_4 coordination active sites, which show encouraging performance in catalyzing ORR, are hailed as the frontier design of M-N-C single atom catalysts for the ORR [23–25]. Nevertheless, great property gap still exists between Fe_{SA}-N-C electrocatalysts and platinum-based benchmarks in consideration of that the electron distribution in the Fe-N_4 structure is symmetric, which leads to the discontented

---

* Corresponding author.
  E-mail address: attsun99@ustb.edu.cn (T. Sun).

adsorption/desorption barrier of Fe-N_4 for oxygen intermediates. With the purpose of boosting the overall ORR activity of Fe_{SA}-N-C catalysts, many strategies have been exploited to enhance the intrinsic ORR activity of single Fe-N_4 sites. Incorporating secondary metal center into Fe_{SA}-N-C catalysts to generate diatomic metal sites has been demonstrated to be an effective approach to realize the above target, owing to that the symmetry of electronic configuration around the Fe-N_4 sites can be disrupted and the adsorptive/desorptive energies for ORR reaction intermediates can be optimized by the synergistic effect between double metal active components [26–31]. Several studies have revealed that Cu single atom electrocatalysts containing atomic Cu-N_4 sites can also perform attractive ORR activity and stability associated with the fact that the dense electron density and high redox potential of Cu can weaken O-O bond [32–35]. Thus, introducing isolated Cu-N_4 centers to Fe_{SA}-N-C catalysts to form FeCu diatomic site catalyst is expected to compensate for the shortage of single Fe-N_4 atomic sites and simultaneously hold the merits of both [27,36–39].

At the same time, to confine and stabilize isolated single atomic sites, carriers are commonly needed. An ideal carrier is preferably to be constructed with hierarchically porous structure to improve the accessibility to atomic metal active sites and facilitate mass transfer throughout the electrode [40,41]. Metal-organic frameworks (MOF) constructed by well aligned organic linkers and atomically dispersed metal species have gained attention because of their high porosity, textural variety, and large surface area. In addition, pyrolyzing MOFs can produce N-doped carbon (NC) frameworks with highly porous structure and abundant surface anchoring sites, which can serve as favorable carriers for single atom catalysts [42]. Thus, embedding Fe and Cu dual single atomic sites in MOFs-derived NC matrix possibly form novel cooperative ORR active sites for dramatically boosting electrocatalytic performance. However, it remains rarely discussed on the fabrication and study of atomically distributed FeCu double sites anchored MOFs-derived NC support, and the affecting mechanism of the integrated FeCu diatomic sites on the ORR behavior still vague.

Herein, we prepared a FeCu asymmetric diatomic site ORR electrocatalyst containing single atomic Fe-N_4 and Cu-N_4 sites co-anchored in the MOF-derived porous NC substrate through a feasible post-adsorption cooperative two-step pyrolysis strategy. Single Fe atomic sites embedded in highly porous NC matrix (Fe_{SA}/NC) was firstly synthesized by pyrolysis of Fe-implanted MOF. Subsequently, co-anchoring of atomically distributed Fe-N_4 sites and Cu-N_4 sites on NC framework ($Fe_{SA}Cu_{SA}$/NC) was produced by chemical adsorption of CuPc and secondary pyrolysis process. Compared with single atom Fe_{SA}/NC and Cu_{SA}/NC catalysts, and benchmark Pt/C catalyst, the resultant Fe_{SA}-Cu_{SA}/NC electrocatalyst presents significantly enhanced ORR activity in 0.1 M $HClO_4$ electrolyte with a half-wave potential ($E_{1/2}$) of 0.86 V and 0.1 M KOH electrolyte ($E_{1/2}$ =0.88 V) as well as superb durability. Theoretical calculation results unveil that the $Fe_{SA}Cu_{SA}$/NC catalyst with particular coordination configuration and appropriate electron redistribution between Fe_{SA}-N_4 and Cu_{SA}-N_4 sites possesses a synergistic effect in decreasing the energy barriers of ORR process, thus contributing to the excellent catalytic performance towards ORR. Importantly, when the $Fe_{SA}Cu_{SA}$/NC catalyst was employed in the application of batteries, the assembled H_2/O_2 fuel cell and Zn-air battery present splendid performance with large peak power density.

2. Experimental

2.1. General remarks

Ethanol (EtOH, 99.7%), methanol (MeOH, 99.7%), N,N-dimethylformamide (DMF, ≥GR), zinc nitrate hexahydrate (Zn$(NO_3)_2$·6 H_2O, 98%), iron nitrate nonahydrate (Fe$(NO_3)_3$·9 H_2O, 99%), potassium hydroxide (KOH, 99.9%), zinc acetate (Zn(Ac)$_2$, 98%), isopropyl alcohol (IPA, ≥99.7%) and potassium chloride (KCl, 99.9%) were supplied by Sinopharm Chemical Reagent Co Ltd. 2-methylimidazole

(MeIM, 99%) was purchased from Macklin. Concentrated sulfuric acid (95%~98%) was procured from Alfa Aesar. Copper phthalocyanine (CuPc, 93%), cobalt phthalocyanine (CoPc, 95%), nickel phthalocyanine (NiPc, 93%), manganese phthalocyanine (MnPc, 98%) and indium phthalocyanine (MnPc, 95%) were purchased from Shanghai Macklin Biochemical Technology Co., Ltd. Perchloric acid ($HClO_4$, 95.0–98.0%) was obtained from Beijing Chemical Works, China. O_2 gas of 99.995% in purity was provided by Suzhou Jinhong Gas Co., Ltd. Pt/C catalyst (20 wt%, HiSPEC-3000, Johnson Matthey) was purchased from Alfa Aesar. Nafion solution were purchased from Sigma-Aldrich. All chemicals were used as received.

2.2. Synthesis of NC

1.97 g 2-MeIM was dissolved in 80 mL methanol, which was subsequently added slowly into 80 mL methanol containing 1.695 g Zn$(NO_3)_2$·6 H_2O while stirring. The ZIF-8 was then obtained by stirring for 12 h and standing for another 12 h at 60 ℃ with reflux. The as-obtained precipitates were centrifuged and washed with methanol for several times and dried in a vacuum oven at 70 ℃ overnight. Finally, the sample was placed in a tube furnace and heated to 900 ℃ for 3 h in a stream of N_2 to yield NC.

2.3. Synthesis of Fe_{SA}/NC

1.97 g 2-MeIM was dissolved in 120 mL methanol, which was subsequently added slowly into 120 mL methanol containing 1.70 g Zn$(NO_3)_2$·6 H_2O and 60 mg Fe$(NO_3)_3$·9 H_2O while stirring. The Fe adsorbed ZIF-8 grew under static at 60 ℃ for 12 h and then stirred for another 12 h with reflux. The as-obtained precipitates were centrifuged and washed with methanol for several times and dried in a vacuum oven at 70 ℃ overnight. Finally, the sample was placed in a tube furnace and heated to 900 ℃ for 3 h in a stream of N_2 to yield Fe_{SA}/NC.

2.4. Synthesis of Cu_{SA}/NC

In a typical procedure, firstly, 20 mg copper phthalocyanine (CuPc) was dissolved in 15 mL concentrated H_2SO_4 and stirred for 1 h under room temperature to obtain a homogeneous solution. Then, 100 mg of NC was added slowly into the above solution and continued to stir for 6 h. Finally, 100 mL of 0 ℃ cold pure water was poured rapidly onto the mixture while tempestuously agitating. The resulting precipitated black composite was filtered and washed sufficiently by 300 mL of deionized water and 100 mL of ethanol until the filter liquor is transparent and clear, then the obtained composite was dried at 70 ℃ for 12 h in a vacuum oven. The as-prepared composite (CuPc-NC) was transferred into a porcelain combustion boat and treated with an annealing process. The composite was first preheated at 150 ℃ for 1 h with a ramping rate of 3 ℃ min^{-1}, and then heated to 900 ℃ with a ramping rate of 5 ℃ min^{-1} and maintained at 900 ℃ for 2 h under nitrogen flow. Finally, after cooling down to room temperature, the Cu_{SA}/NC powders were acquired.

2.5. Synthesis of $Fe_{SA}Cu_{SA}$/NC

20 mg copper phthalocyanine (CuPc) was dissolved in 15 mL concentrated H_2SO_4 and stirred for 1 h under room temperature to obtain a homogeneous solution. Then, 100 mg of Fe_{SA}/NC was added slowly into the above solution and continued to stir for 6 h. Finally, 100 mL of 0 ℃ cold pure water was poured rapidly onto the mixture while tempestuously agitating. The resulting precipitated black composite was filtered and washed sufficiently by 300 mL of deionized water and 100 mL of ethanol until the filter liquor is transparent and clear, then the obtained composite was dried at 70 ℃ for 12 h in a vacuum oven. The as-prepared composite (CuPc-Fe_{SA}/NC) was transferred into a porcelain combustion boat and treated with an annealing process. The composite

was first preheated at 150 °C for 1 h with a ramping rate of 3 °C min^{-1}, and then heated to 900 °C with a ramping rate of 5 °C min^{-1} and maintained at 900 °C for 2 h under nitrogen flow. Finally, after cooling down to room temperature, the $Fe_{SA}Cu_{SA}/NC$ powders were acquired.

2.6. Synthesis of $Fe_{SA}M_{SA}/NC$ (M= Co, Ni, Mn and In)

Metal phthalocyanine (MPc) was dissolved in 15 mL concentrated H_2SO_4 and stirred for 1 h under room temperature to obtain a homogeneous solution. Then, 100 mg of Fe_{SA}/NC was added slowly into the above solution and continued to stir for 6 h. Finally, 100 mL of 0 °C cold pure water was poured rapidly onto the mixture while tempestuously agitating. The resulting precipitated black composite was filtered and washed sufficiently by 300 mL of deionized water and 100 mL of ethanol until the filter liquor is transparent and clear, then the obtained composite was dried at 70 °C for 12 h in a vacuum oven. The as-prepared composite (MPc-Fe_{SA}/NC) was transferred into a porcelain combustion boat and treated with an annealing process. The composite was first preheated at 150 °C for 1 h with a ramping rate of 3 °C min^{-1}, and then heated to 900 °C with a ramping rate of 5 °C min^{-1} and maintained at 900 °C for 2 h under nitrogen flow. Finally, after cooling down to room temperature, the $Fe_{SA}M_{SA}/NC$ powders were acquired.

3. Results and discussion

3.1. DFT calculations

To reveal the effect of adjacent Cu_{SA}-N_4 on the properties of Fe_{SA}-N_4 sites, density functional theory (DFT) calculations were carried out. As shown in Fig. 1a, the adsorption energies for O_2 on Fe_{SA}-N_4 and Fe_{SA}-N_4&Cu_{SA}-N_4 systems are − 1.99 eV and − 2.17 eV, respectively, suggesting a more favorable O_2 adsorption process on Fe_{SA}-N_4&Cu_{SA}-N_4 than that on Fe_{SA}-N_4. Moreover, a slightly higher stretching degree of O-O bond (ca. 1.296 Å) was observed on Fe_{SA}-N_4&Cu_{SA}-N_4 system as compared to the Fe_{SA}-N_4 system (1.294 Å), indicating that the brokage of O_2 molecule on Fe single atom site is feasible, and the brokage of O_2 molecule on Fe_{SA}-N_4&Cu_{SA}-N_4 site is even easier. To further investigate the impact of Cu_{SA}-N_4 on the Fe_{SA}-N_4 site for OOH* adsorption, the projected density of states (PDOS) calculations was carried out for the

d orbitals of Fe and *p* orbital of O for Fe_{SA}-N_4 and Fe_{SA}-N_4&Cu_{SA}-N_4 after OOH* adsorption, respectively. As depicted in Fig. 1b, for OOH bonding on Fe site in pristine Fe_{SA}-N_4, the frontier orbitals for Fe-O bonding are mainly π * anti-bonding orbitals, resulting in a relatively weak Fe-OOH bonding. In contrast, the introduction of Cu_{SA}-N_4 varies the orbital energy levels and spatial distributions of Fe 3*d* orbitals, making the original $π_2$ * anti-bonding orbitals become π bonding orbitals by the rehybridization of Fe d_z^2 and O *p* orbitals. This thus strengthens the Fe-O bond. Fig. 1c show the PDOS for the *d* orbitals of Fe and *p* orbital of O for Fe_{SA}-N_4 and Fe_{SA}-N_4&Cu_{SA}-N_4 after OH* adsorption, respectively. Clearly, with surrounding Cu_{SA}-N_4, the Fe d_{xy} and O *p* orbitals can form $π_1$ bond, and the Fe d_{xy}, $d_{x^2-y^2}$ and O *p* orbitals can form $π_2$ bond. These additional bonding orbitals thereby strengthen the Fe-OH* bonding. Therefore, we assume that the enhancement of ORR activity of Fe_{SA}-N_4&Cu_{SA}-N_4 mainly originate from the electronic orbitals modulation of Fe_{SA}-N_4 by Cu_{SA}-N_4 [43–45].

### 3.2. Materials synthesis and characterization

As guided by the DFT calculation results of ORR performance of Fe_{SA}-N_4 with or without surrounding Cu, Fe and Cu single atom catalysts, as well as FeCu diatomic sites catalyst were fabricated through a well-designed strategy. The synthetic procedure of the $Fe_{SA}Cu_{SA}/NC$ catalyst was schematically illustrated in Fig. 2a, consisting of the fabrication of the Fe^{3+} implanted zeolitic imidazolate framework (ZIF-8), chemical adsorption of CuPc, and two step pyrolysis. Specifically, the Fe^{3+}-implanted ZIF-8 was synthesized by static handling and following stirring the mixture of $Zn(NO_3)_2\cdot 6 H_2O$, $Fe(NO_3)_3\cdot 9 H_2O$, 2-MeIM, and methanol, and subsequently was pyrolyzed to acquire porous Fe_{SA}/NC. Next, the as-prepared Fe_{SA}/NC was acted as the host for subsequently adsorbing Cu species, which was realized by the impregnation of Fe_{SA}/NC into CuPc dissolved concentrated sulfuric acid. Finally, the $Fe_{SA}Cu_{SA}/NC$ catalyst was produced via secondly pyrolyzing CuPc adsorbed Fe_{SA}/NC.

The transmission electron microscopy (TEM) image in Fig. 2b shows the polyhedral morphology of $Fe_{SA}Cu_{SA}/NC$ with rough surface. Compared with the morphology of NC, the morphologies of Fe_{SA}/NC, Cu_{SA}/NC and $Fe_{SA}Cu_{SA}/NC$ do not show discernible change in the TEM observations, indicating the negligible influence of the introduction of
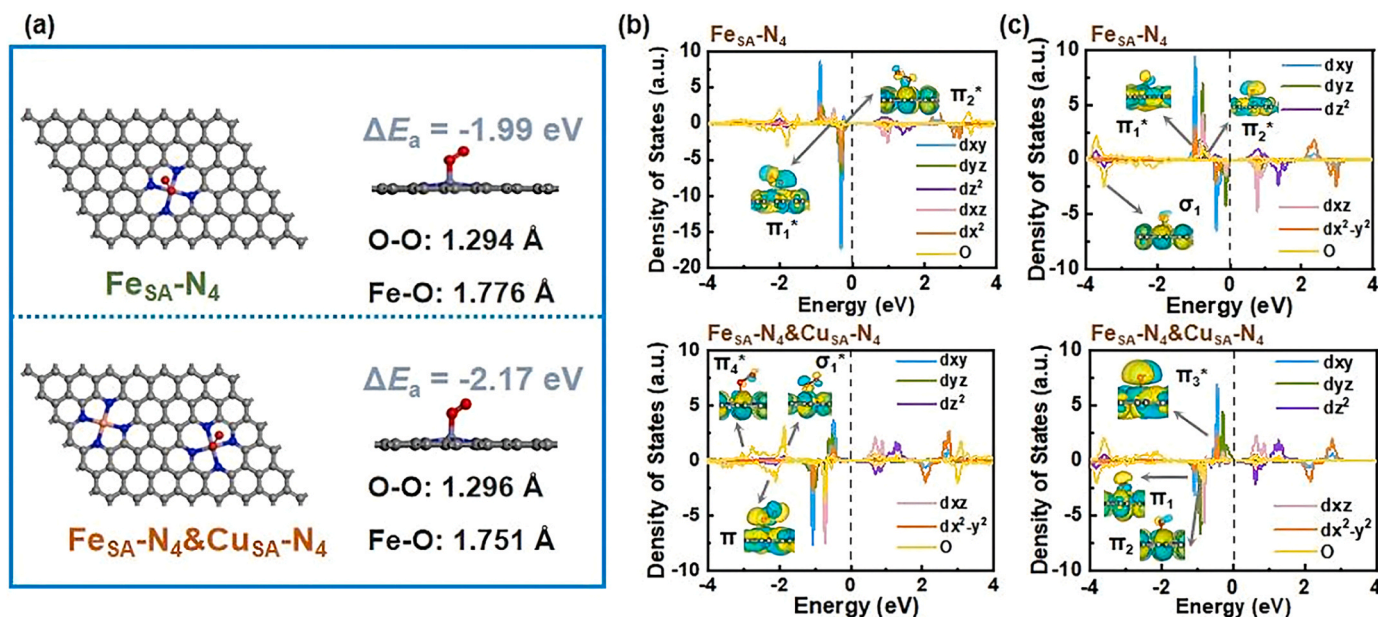
Fig. 1. (a) O_2 adsorption models of Fe_{SA}-N_4 and Fe_{SA}-N_4&Cu_{SA}-N_4. (b) Computed projected density of states of Fe_{SA}-N_4 and Fe_{SA}-N_4&Cu_{SA}-N_4 after OOH* adsorption. (c) Computed projected density of states of Fe_{SA}-N_4 and Fe_{SA}-N_4&Cu_{SA}-N_4 after OH* adsorption (σ and π represent the bonding molecular orbitals between *d* orbital of Fe and *p* orbital of O. σ * and π * represent the antibonding molecular orbitals between *d* orbitals of Fe and *p* orbital of O).
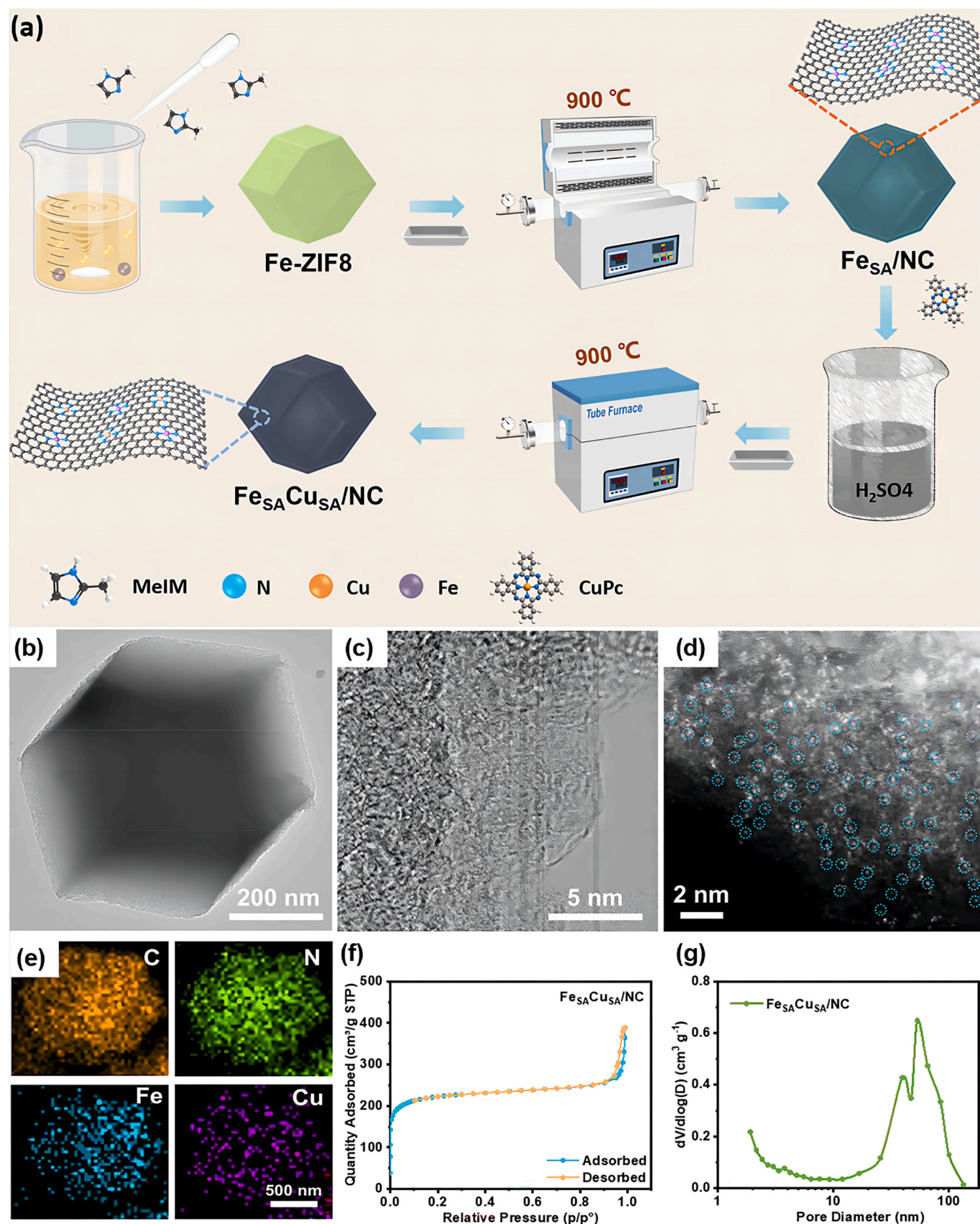
Fig. 2. (a) Schematic illustration of the synthesis of the $Fe_{SA}Cu_{SA}/NC$ photocatalyst. (b) TEM image of $Fe_{SA}Cu_{SA}/NC$. (c) High-resolution TEM image of $Fe_{SA}Cu_{SA}/NC$. (d) AC HAADF-STEM image of $Fe_{SA}Cu_{SA}/NC$. Single Fe or Cu atoms are highlighted by dashed green circles. (e) EDS mapping images of $Fe_{SA}Cu_{SA}/NC$. (f) N_2 adsorption-desorption isotherms and (g) Pore-size distribution curve of $Fe_{SA}Cu_{SA}/NC$.

metal species on the morphology of NC support (Fig. S1). The high-resolution TEM image in Fig. 2c indicates that the surface of Fe_{SA}-Cu_{SA}/NC polyhedron is covered by a thin CN layer. As shown in Fig. 2d, the aberration-corrected high-angle annular dark-field scanning transmission electron microscopy (AC HAADF-STEM) image of $Fe_{SA}Cu_{SA}$/NC, which exhibits abundant bright dots marked by dashed green cycles, reveals the isolated single atomic dispersion of Fe and Cu atoms on the porous NC matrix. Energy-dispersive X-ray spectroscopy (EDS) mapping images indicate that there is no existence of obvious metal nanoparticles, and Fe and Cu species are uniformly spread over the surface of porous NC support (Fig. 2e). Moreover, the Cu_{SA}/NC, Fe_{SA}/NC, Fe_{SA}-Co_{SA}/NC, $Fe_{SA}Ni_{SA}$/NC, $Fe_{SA}Mn_{SA}$/NC, and $Fe_{SA}In_{SA}$/NC catalysts were also prepared as control samples (Figs. S2-S8). Inductively coupled plasma-mass spectrometry (ICP-MS) was operated to measure the contents of metal species in $Fe_{SA}Cu_{SA}$/NC, Fe_{SA}/NC, and Cu_{SA}/NC samples. The Fe content and Cu content were determined to be 0.88 wt% and 1.35 wt% in $Fe_{SA}Cu_{SA}$/NC, respectively (Table S1). The Fe content in Fe_{SA}/NC and Cu content in Cu_{SA}/NC were identified to be 1.12 and 1.58 wt%, respectively. N_2 adsorption–desorption isotherms in Fig. 2f demonstrate a high Brunauer–Emmett–Teller (BET) surface area of 795.2 m^2 g^{-1} for $Fe_{SA}Cu_{SA}$/NC with porous structure. The calculated surface area of microporous and mesoporous are 608.7 m^2 g^{-1} and 125.6 m^2 g^{-1}, respectively. The pore size distribution curve verified the presence of abundant macropores in $Fe_{SA}Cu_{SA}$/NC (Fig. 2g), which is important to largely promote the mass transport to and from the FeCu diatomic active sites, thus improving the catalytic kinetics.

X-ray photoelectron spectroscopy (XPS) tests were fulfilled to reveal the surface composition and chemical structure of $Fe_{SA}Cu_{SA}$/NC, Fe_{SA}/NC, and Cu_{SA}/NC (Fig. 3, Fig. S10 and Fig. S11). In the high-resolution Fe 2p spectrum of $Fe_{SA}Cu_{SA}$/NC (Fig. 3a), the peaks for Fe $2p_{3/2}$ and Fe $2p_{1/2}$ at the binding energies (BEs) of 721.05 eV and 710.82 eV, respectively, are characteristic of Fe^{2+} in $Fe_{SA}Cu_{SA}$/NC. The left shift of the BEs of Fe $2p_{3/2}$ and Fe $2p_{1/2}$ peaks in Fe 2p spectrum of $Fe_{SA}Cu_{SA}$/NC compared with that in Fe 2p spectrum of Fe_{SA}/NC indicates the electron delocalization of Fe species resulted from the introduction of Cu species.

As shown in the high-resolution Cu 2p spectrum of $Fe_{SA}Cu_{SA}$/NC (Fig. 3b), the peaks for Cu $2p_{3/2}$ and Cu $2p_{1/2}$ at the BEs of 952.40 eV and 932.47 eV, respectively, are characteristic of Cu^{2+} in $Fe_{SA}Cu_{SA}$/NC. Three main peaks in the deconvoluted C 1s high resolution XPS spectrum of $Fe_{SA}Cu_{SA}$/NC (Fig. 3c) correspond to C=C (283.91 eV), C=N (285.37 eV) and C-N (286.31 eV), respectively. The high-resolution N 1s spectrum (Fig. 3d) reveals the co-existence of four types of N, namely graphitic-N (401.06 eV), pyrrolic-N (399.72 eV), pyridinic-N (398.59 eV), and oxidized-N (402.43 eV).

To probe the chemical information and coordination microenvironment of the Fe and Cu at the atomic level in the $Fe_{SA}Cu_{SA}$/NC catalyst, synchrotron radiation-based X-ray absorption fine structure (XAFS) characterization was further analyzed. The normalized Fe K-edge XANES (X-ray absorption near-edge structure) spectra of $Fe_{SA}Cu_{SA}$/NC, Fe_{SA}/NC and two reference samples of Fe foil and FePc were comparatively analyzed in Fig. 4a. We observed that the near-edge absorption positions of $Fe_{SA}Cu_{SA}$/NC and Fe_{SA}/NC lie higher than that of Fe foil and locate closely to that of FePc, indicating that Fe atoms in $Fe_{SA}Cu_{SA}$/NC and Fe_{SA}/NC are positively charged with about + 2 oxidation state, in agreement with the XPS analysis. Meanwhile, the Cu K-edge XANES spectra of $Fe_{SA}Cu_{SA}$/NC, Cu_{SA}/NC, Cu foil, and CuPc in Fig. 4f also reveal the similar results, and the average oxidation state of Cu element in $Fe_{SA}Cu_{SA}$/NC and Cu_{SA}/NC is also about + 2. In the k^3-weighted Fourier transform extended X-ray absorption fine structure (FT-EXAFS) spectra of Fe K-edge in both $Fe_{SA}Cu_{SA}$/NC and Fe_{SA}/NC samples, only one prominent characteristic peak located at around 1.5 Å can be seen at R space, which can be ascribed to the Fe-N scattering by combining with the analysis of Fe foil and FePc spectra (Fig. 4b). In addition, the R-space of $Fe_{SA}Cu_{SA}$/NC catalyst (2.06 Å) is higher than that Fe_{SA}/NC catalyst (2.00 Å) (Table S2), illustrating that the coordination configuration of Fe atoms in the $Fe_{SA}Cu_{SA}$/NC catalyst is changed. Similarly, in the Cu K-edge FT-EXAFS spectra (Fig. 4g), the dominant peaks at around 1.5 Å in $Fe_{SA}Cu_{SA}$/NC and Cu_{SA}/NC can correspond to the Cu-N bond according to the CuPc spectrum. Compared with the Fe foil and Cu foil curves, the missing of Fe-Fe scattering signal at around 2.2 Å and Cu–Cu scattering
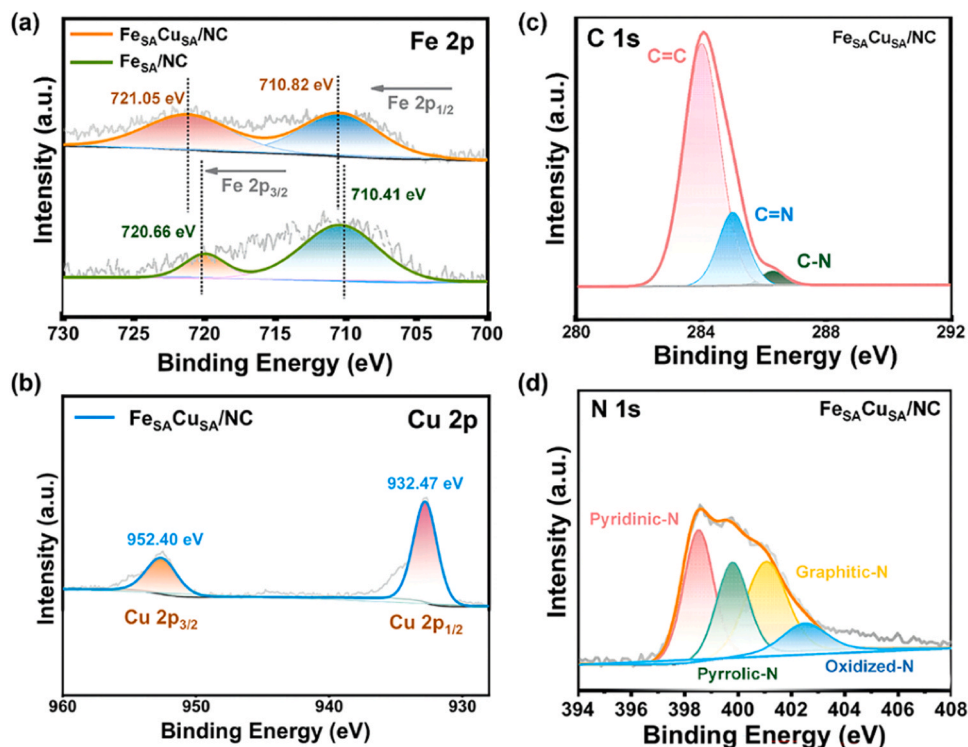
Fig. 3. High resolution XPS (a) Fe 2p spectra of $Fe_{SA}Cu_{SA}$/NC and Fe_{SA}/NC, (b) Cu 2p spectrum of $Fe_{SA}Cu_{SA}$/NC, (c) C 1s spectrum of $Fe_{SA}Cu_{SA}$/NC, and (d) N 1s spectrum of $Fe_{SA}Cu_{SA}$/NC.
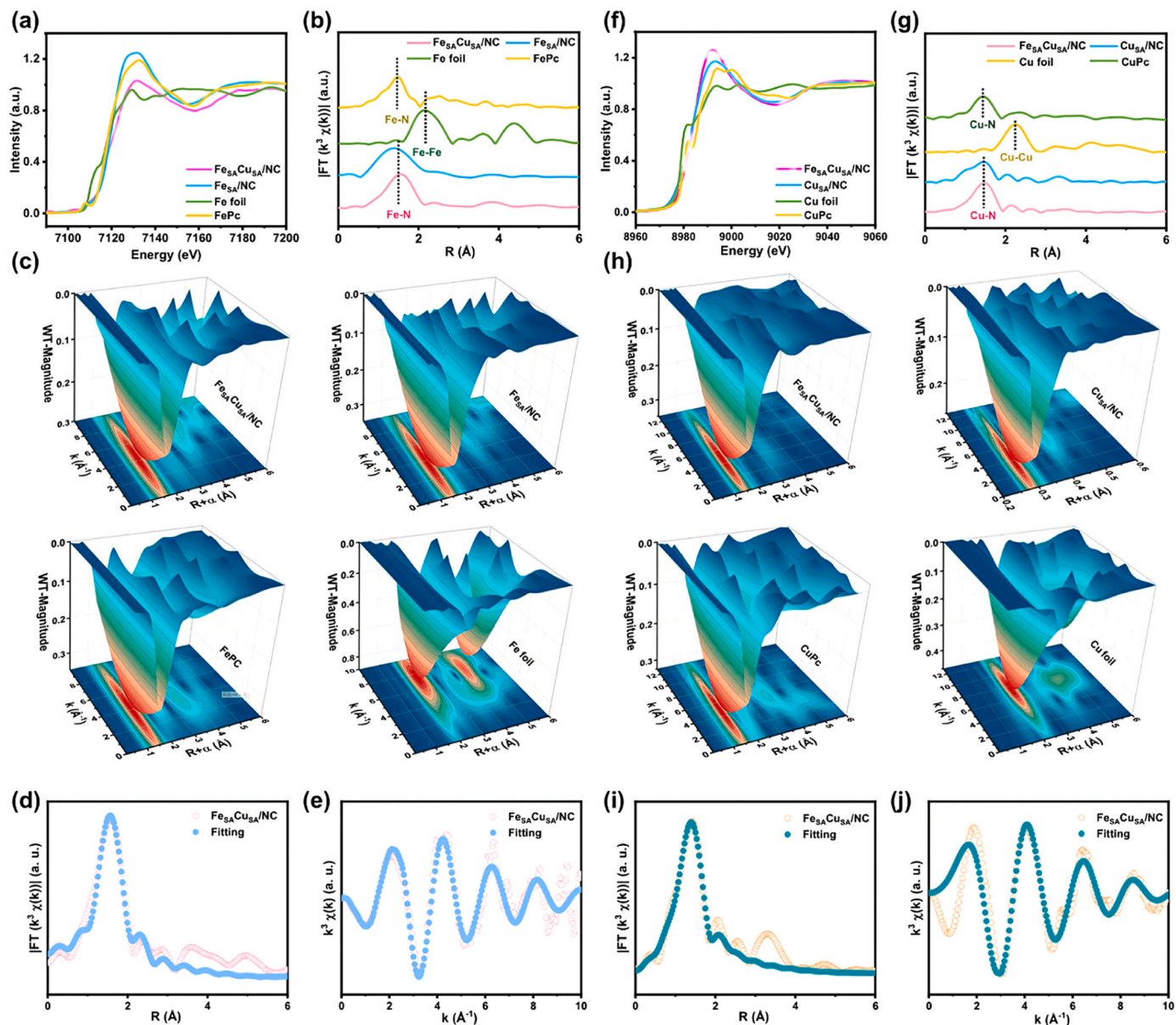
Fig. 4. (a) XANES spectra, (b) FT-EXAFS spectra, and (c) WT-EXAFS spectra of $Fe_{SA}Cu_{SA}/NC$, Fe_{SA}/NC, FePc and Fe foil. (d) and (e) The fitted Fe K-edge EXAFS curves of $Fe_{SA}Cu_{SA}/NC$ at r space and k space. (f) XANES spectra, (g) FT-EXAFS spectra, and (h) WT-EXAFS spectra of $Fe_{SA}Cu_{SA}/NC$, Cu_{SA}/NC, CuPc, and Cu foil. (i) and (j) The fitted Cu K-edge EXAFS curves of $Fe_{SA}Cu_{SA}/NC$ at k space and r space.

signal at around 2.3 Å confirms the atomic-level distribution of Fe and Cu and the presence of FeCu diatomic site structure in the resultant $Fe_{SA}Cu_{SA}/NC$ catalyst [41].

To further verify the single atomic dispersion of Fe and Cu species, the EXAFS wavelet transform (WT) analysis was conducted, which is another important technique to distinguish backscattering atoms by offering contrastive results regarding the radial distance resolution in k-space. The WT contour plots of $Fe_{SA}Cu_{SA}/NC$, Fe_{SA}/NC, Cu_{SA}/NC, and various reference samples were recorded in Figs. 4c and 4h. The strong oscillation signal at around 4.3 Å^{-1} shown in $Fe_{SA}Cu_{SA}/NC$ and Fe_{SA}/NC is close to that of FePc and obviously distinct from Fe foil, demonstrating the existence of single atomic Fe-N centers. Similarly, $Fe_{SA}Cu_{SA}/NC$ and Cu_{SA}/NC show only one strong oscillation signal at 4.6 Å^{-1} assigned to Cu-N coordination, distinctly different from Cu foil, further indicating the atomically distributed mode of Cu species. To further investigate the coordination structure of Fe and Cu atoms in $Fe_{SA}Cu_{SA}/NC$, quantitative FT transformed EXAFS fitting was carried out in R and k space. As can be observed in the fitting plots (Figs. 4d, 4e, 4i and 4j) and the obtained

fitting data (Table S2 and Table S3), in the first shell of $Fe_{SA}Cu_{SA}/NC$ catalyst, the central Fe atoms are averagely coordinated by four N atoms at bond length of 2.06 Å to form atomic Fe_{SA}-N_4 configuration, and the central Cu atoms are also averagely coordinated by four N atoms with bond length of 1.95 Å to form atomic Cu-N_4 configuration These results prove the coexisting Fe–N_4 and Cu-N_4 single atom moieties in $Fe_{SA}Cu_{SA}/NC$ more deeply.

3.3. Electrochemical measurements in flow cell

The electrochemical ORR performances of the as-prepared $Fe_{SA}Cu_{SA}/NC$ and some control samples were first examined in O_2-saturated acidic media (0.1 M $HClO_4$) using rotating disk electrode (RDE) with a three-electrode system [46]. Fig. 5a shows the linear sweep voltammetry (LSV) curves of various catalysts at 1600 rpm. It can be seen that the $Fe_{SA}Cu_{SA}/NC$ catalyst possesses the best ORR activity among all the studied catalysts with a positive half-wave potential ($E_{1/2}$) of 0.86 V, which is higher than that of Cu_{SA}/NC ($E_{1/2}$ =0.77 V), Fe_{SA}/NC ($E_{1/2}$
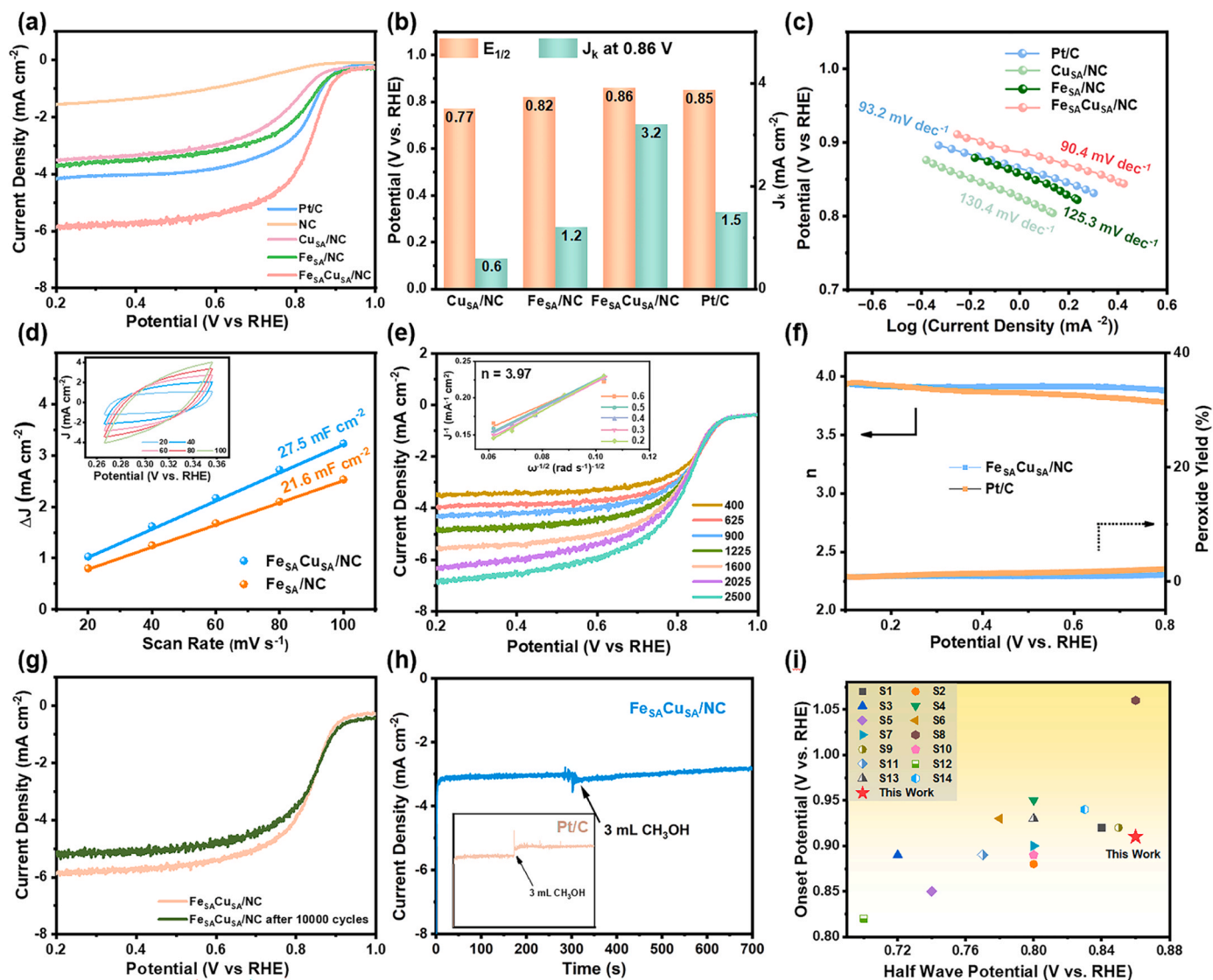
Fig. 5. (a) ORR polarization curves of different catalysts in O_2-saturated 0.1 M $HClO_4$ at the rotating rate of 1600 rpm (scan rate: 5 mV s^{-1}). (b) Comparison of $E_{1/2}$ and J_k at 0.86 V and (c) Tafel plots of Pt/C, Cu_{SA}/NC, Fe_{SA}/NC and $Fe_{SA}Cu_{SA}$/NC. (d) Evaluation of C_{dl} values for Fe_{SA}/NC and $Fe_{SA}Cu_{SA}$/NC by plotting the ΔJ vs. scan rate. Inset: CV curves for $Fe_{SA}Cu_{SA}$/NC at various scan rates toward ORR. (e) ORR polarization curves of $Fe_{SA}Cu_{SA}$/NC in 0.1 M $HClO_4$ at different rotating rates (400–2500 rpm). Inset: K-L plots of $Fe_{SA}Cu_{SA}$/NC at different potentials. (f) Electron-transfer number (*n*) and H_2O_2 yield vs. potential of $Fe_{SA}Cu_{SA}$/NC and Pt/C. (g) ORR polarization curves of $Fe_{SA}Cu_{SA}$/NC initially and after 10000 cycles in O_2-saturated 0.1 M $HClO_4$ at a scan rate of 100 mV s^{-1}. (h) Methanol tolerance evaluation for $Fe_{SA}Cu_{SA}$/NC and Pt/C at 0.6 V vs. RHE with 3 mL methanol addition in 0.1 M $HClO_4$ electrolyte at around 300 s (i) Comparison of the ORR activities between $Fe_{SA}Cu_{SA}$/NC and literature examples at 1600 rpm in acidic medium (the references inside the Fig. are listed in the Supporting Information).

=0.82 V), and commercial Pt/C ($E_{1/2}$ =0.85 V). At the same time, negligible catalytic activity of metal-free pure NC catalyst toward ORR can be observed, implying the crucial role of atomic Fe moieties and/or atomic Cu moieties in boosting ORR activity [47]. Moreover, the obtained ORR limiting current density of $Fe_{SA}Cu_{SA}$/NC is as large as 5.8 mA cm^{-2}, much better than that of Pt/C (4.1 mA cm^{-2}), which can be attributed to the superior conductivity of the porous carbon structure with boosted mass/charge transfer. The ORR kinetic current density (J_k) of Fe_{SA}/NC at 0.86 V was calculated to be 1.2 mA cm^{-2}, which is lower than that of Pt/C (1.5 mA cm^{-2}). By introducing single Cu atoms in Fe_{SA}/NC catalyst, the $Fe_{SA}Cu_{SA}$/NC catalyst with Fe-N_4 and Cu-N_4 diatomic sites is produced and exhibits a significantly improved ORR J_k of 3.2 mA cm^{-2} at 0.86 V, which is almost triple the value of Fe_{SA}/NC and twice the value of Pt/C, demonstrating that the presence of single Cu-N_4 centers has a company influence in enhancing the electrocatalytic activity for ORR (Fig. 5b). As shown in Fig. 5c, the more satisfactory reaction kinetics of Fe_{SA}/NC is also verified by its smallest Tafel plot

slope (90.4 mV dec^{-1}), in comparison with that of Fe_{SA}/NC (125.3 mV dec^{-1}), Cu_{SA}/NC (130.4 mV dec^{-1}) and Pt/C (93.2 mV dec^{-1}). The electrochemical active surface area (ECSA) is another criterion used for assessing catalytic activity of the electrocatalyst for ORR, while the double-layer capacitances (C_{dl}) value can directly reflects the ECSA. Here, cyclic voltammetry (CV) was carried out at scan rate of 20–100 mV s^{-1} to obtain C_{dl} (Fig. 5d). The calculated C_{dl} of $Fe_{SA}Cu_{SA}$/NC is 25.1 mF cm^{-2}, which is higher than that of Fe_{SA}/NC (22.9 mF cm^{-2}). This result shows that $Fe_{SA}Cu_{SA}$/NC possesses rich effective active sites, which can contribute remarkably to the boosted ORR activity. Rotating disk electrode (RDE) tests on $Fe_{SA}Cu_{SA}$/NC were carried out at varying rotation speeds to gain more in-depth understanding of the electrocatalytic kinetics towards ORR.

The Koutecky–Levich (K-L) plots extracted from the RDE tests display remarkable linearity, implying the first-order reaction kinetics (Fig. 5e). The electron transfer number (*n*) at the $Fe_{SA}Cu_{SA}$/NC electrode was calculated to be 3.97 according to the K–L equations, manifesting a

preferred 4e⁻ transfer path during catalyzing ORR. Moreover, the rotating ring-disk electrode (RRDE) measurement was also conducted to further investigate the ORR selectivity of $Fe_{SA}Cu_{SA}/NC$. The results clearly indicate that the $Fe_{SA}Cu_{SA}/NC$ catalyst has a rather low hydrogen peroxide (H_2O_2) yield below 2.5% at 0.1–0.8 V and an average n value of around 3.97 (Fig. 5f), which is in correspondence with the results obtained based on K–L plots [48]. Stability is also an important factor in the evaluation of a practical electrocatalyst. The stability of $Fe_{SA}Cu_{SA}/NC$ was examined by an accelerated durability test (ADT). As shown in Fig. 5g, after 10,000 continuous CV cycles at a scan rate of 100 mV s^{-1}, the $E_{1/2}$ of $Fe_{SA}Cu_{SA}/NC$ shows almost no attenuation compared with the $E_{1/2}$ value before cycling test, demonstrating the superior stability of $Fe_{SA}Cu_{SA}/NC$ in ORR catalysis. Furthermore, the methanol tolerance property of $Fe_{SA}Cu_{SA}/NC$ was investigated by suddenly injecting 3 mL methanol into the O_2 saturated 0.1 M $HClO_4$ electrolyte at 300 s during the potentiostatic test (I-t). When infusing methanol during ORR, the current density of $Fe_{SA}Cu_{SA}/NC$ shows negligible change, while obvious current density variation can be observed on Pt/C electrode (Fig. 5h), proving an outstanding methanol resistance of $Fe_{SA}Cu_{SA}/NC$. Moreover, the ORR catalytic activities of $Fe_{SA}Co_{SA}/NC$, $Fe_{SA}Ni_{SA}/NC$, $Fe_{SA}Mn_{SA}/NC$, and $Fe_{SA}In_{SA}/NC$ were also investigated and compared with that of $Fe_{SA}Cu_{SA}/NC$. The LSV curves shown in Fig. S12 reveal that the $Fe_{SA}Cu_{SA}/NC$ features the optimal ORR activity among these catalysts in terms of $E_{1/2}$ and limiting current density, implying the great significance of the introduction of Cu sites into Fe_{SA}/NC for boosting the ORR activity of $Fe_{SA}Cu_{SA}/NC$. Impressively, such outstanding ORR activity achieved by $Fe_{SA}Cu_{SA}/NC$ surpasses that of most recently reported advanced ORR electrocatalysts under acidic condition (Fig. 5i and Table S4). The TEM, XRD, XPS, and EDS mapping images of $Fe_{SA}Cu_{SA}/NC$ shown in Fig. S13 disclose that the single-atom form and valence state of Fe and Cu species in the recycled $Fe_{SA}Cu_{SA}/NC$, as well as the morphology of the recycled $Fe_{SA}Cu_{SA}/NC$ are well maintained after the ADT test compared with the original $Fe_{SA}Cu_{SA}/NC$.

Furthermore, the ORR performances of $Fe_{SA}Cu_{SA}/NC$, Fe_{SA}/NC, Cu_{SA}/NC, NC, and Pt/C were also tested under alkaline condition (0.1 M KOH) (Fig. 6). As can be seen in Fig. 6a, the $Fe_{SA}Cu_{SA}/NC$ catalyst also displays the optimal ORR activity compared with other contrastive samples with an $E_{1/2}$ of 0.88 V vs. RHE, which is 40 mV higher than that of the benchmark Pt/C (0.84 V). A direct 4e⁻ transfer route toward ORR was proved for $Fe_{SA}Cu_{SA}/NC$ catalyst according to the K–L plots obtained in the potential from 0.4 to 0.8 V vs. RHE (Fig. 6b). The $Fe_{SA}Cu_{SA}/NC$ catalyst also exhibits a significantly high ORR J_k of 4.3 mA cm^{-2} at 0.88 V, which is much higher than that of Pt/C, demonstrating its boosted electrocatalytic activity for ORR (Fig. 6c). In addition, the pretty low H_2O_2 yield below 3% and the average n of about 3.99 for the $Fe_{SA}Cu_{SA}/NC$ catalyst acquired based on the RRDE measurements conducted from 0.2 to 0.8 V vs. RHE further demonstrate the 4e⁻ ORR pathway (Fig. 6d), which is in good agreement with the findings of K–L equation. After the ADT test for 10,000 successive CV cycles, the $Fe_{SA}Cu_{SA}/NC$ exhibits negligible decay in $E_{1/2}$, confirming that the $Fe_{SA}Cu_{SA}/NC$ catalyst also has a splendid stability under alkaline conditions (Fig. 6e). At the same time, the $Fe_{SA}Cu_{SA}/NC$ catalyst also shows a remarkable capacity for methanol-tolerance (Fig. 6f). Based on the above all results, the superb ORR catalytic performances of $Fe_{SA}Cu_{SA}/NC$ in both acidic and alkaline medium can be attributed to the coexistence of single atomic Fe-N$_4$ sites and Cu-N$_4$ active sites for simultaneously enhancing ORR property, as well as the highly porous carbon matrix with favorable mass/charge diffusion for significantly improving the electrical conductivity and active site exposure.

3.4. Mechanistic insights

To unveil more insights into the cooperative effects of Fe_{SA}-N$_4$ and Cu_{SA}-N$_4$ atomic sites on the ORR mechanism of $Fe_{SA}Cu_{SA}/NC$, further DFT calculations were carried out to study the binding energies of ORR
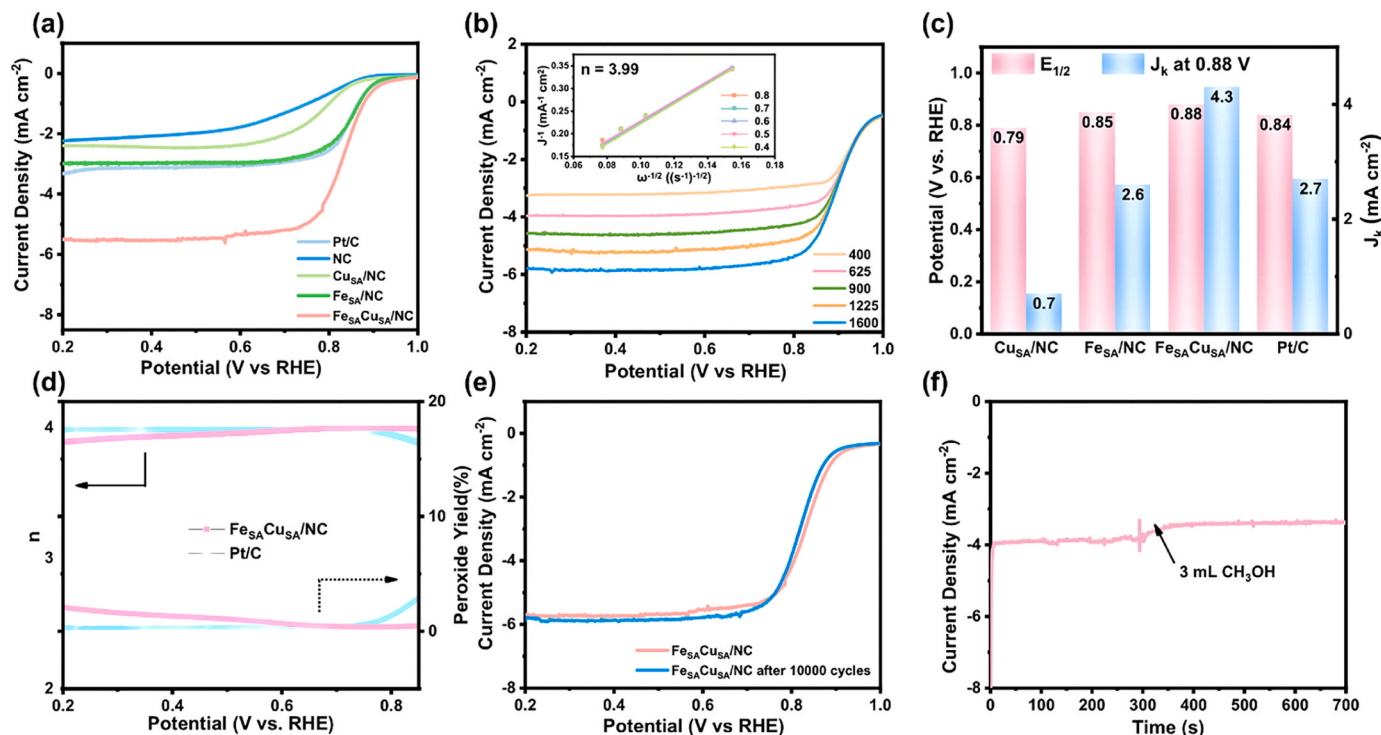
Fig. 6. (a) ORR polarization curves of different catalysts in O_2-saturated 0.1 M KOH at the rotating rate of 1600 rpm (scan rate: 5 mV s^{-1}). (b) Comparison of $E_{1/2}$ and J_k at 0.88 V of Pt/C, Cu_{SA}/NC, Fe_{SA}/NC and $Fe_{SA}Cu_{SA}/NC$. (c) ORR polarization curves of $Fe_{SA}Cu_{SA}/NC$ in 0.1 M KOH at different rotating rates. Inset: K-L plots of $Fe_{SA}Cu_{SA}/NC$ at different potentials. (d) ORR polarization curves of $Fe_{SA}Cu_{SA}/NC$ initially and after 10,000 cycles in O_2-saturated 0.1 M KOH at a scan rate of 100 mV s^{-1}. (e) Electron-transfer number (n) and H_2O_2 yield vs. potential of $Fe_{SA}Cu_{SA}/NC$ and Pt/C. (f) Methanol tolerance evaluation for $Fe_{SA}Cu_{SA}/NC$ at 0.6 V vs. RHE with 3 mL methanol addition in 0.1 M KOH electrolyte at around 300 s.

intermediates and the relevant energy barriers. Three optimized models were built, including single Fe_{SA}-N_4 atomic site (Fe_{SA}/NC), single Cu_{SA}-N_4 atomic site (Cu_{SA}/NC), and single Fe_{SA}-N_4&Cu_{SA}-N_4 atomic site ($Fe_{SA}Cu_{SA}$/NC) on graphene (Fig. S14). Generally, the electrochemical ORR pathway in acidic electrolyte is regarded to include the five steps (Fig. 7a): 1) adsorbing O_2 on the catalytic sites; 2) generating the *OOH intermediate; 3) forming the *O intermediate; 4) forming the *OH intermediate; 5) generating the product of H_2O. The Gibbs free energy diagrams of the four-electron ORR pathway over Fe_{SA}/NC, Cu_{SA}/NC, and $Fe_{SA}Cu_{SA}$/NC under acidic conduction are shown in Fig. 7b [49–52]. The thermodynamical downhill in free energy during the ORR steps occurred on these structural models at zero potential (U=0 V) indicates the spontaneous exothermic features of all reaction pathways. At the equilibrium potential (U=1.23 V), the inital two ORR steps for $Fe_{SA}Cu_{SA}$/NC and Fe_{SA}/NC are downhill and regared as exothermic pathways, indicating the facile breakage of O-O bond as well as *OOH and *O formation. In contrast, the ORR steps of *OOH and *O formation for Cu_{SA}/NC are uphill and identified as endothermic routes. The energy barrier for $Fe_{SA}Cu_{SA}$/NC to accomplish the final electron-transfer step of *OH protonation (the rate-determining step of the ORR proceeds on the three models) was calculated to be 0.69 eV, which is much smaller than that of Fe_{SA}/NC (1.31 eV), resulting in that the needed overpotential for $Fe_{SA}Cu_{SA}$/NC to drive ORR is lower than that for Fe_{SA}/NC. In order to further reveal the fundamental origin of the excellent catalytic activity toward ORR catalyzed by $Fe_{SA}Cu_{SA}$/NC, the electronic configuration of central Fe moieties was studied by conducting calculations of charge density difference (Fig. 7e). In contrast to the Fe atomic site in Fe_{SA}/NC with symmetric electron transfer, the asymmetric FeCu dual atomic site experiences a symmetry destruction of electron transfer, resulting in the electron redistribution in $Fe_{SA}Cu_{SA}$/NC. The smaller charge depletion of Fe atom in $Fe_{SA}Cu_{SA}$/NC than that in Fe_{SA}/NC caused by the electron redistribution of $Fe_{SA}Cu_{SA}$/NC indicates that the charge of centeral Fe atom in $Fe_{SA}Cu_{SA}$/NC is less positive campared with that in Fe_{SA}/NC. The additional electron accumulation on the central Fe atom in $Fe_{SA}Cu_{SA}$/NC contributes to the weakened adsorption capacity of ORR intermediates. These theoretical calculation results reveal that the single Fe_{SA}-N_4&Cu_{SA}-N_4 atomic site in $Fe_{SA}Cu_{SA}$/NC is more active than the single Fe_{SA}-N_4 site in Fe_{SA}/NC and single Cu_{SA}-N_4 atomic site in Cu_{SA}/NC, which significantly contributes to the reduced ORR energy barrier and boosted catalytic property of $Fe_{SA}Cu_{SA}$/NC.

3.5. The performance of $Fe_{SA}Cu_{SA}$/NC in PEMFC and ZAB

The performance of $Fe_{SA}Cu_{SA}$/NC in acidic H_2/O_2 PEMFC was investigated by using $Fe_{SA}Cu_{SA}$/NC as the cathode catalyst (Fig. 8a). The $Fe_{SA}Cu_{SA}$/NC-based membrane electrode assembly (MEA) tests were carried out during practical fuel cell operations under a series of H_2/O_2 backpressures (0.3, 1.0, and 2.0 bar) [53,54]. The polarization and power density plots of PEMFCs obtained at the measurement temperature of 80 °C are shown in Fig. 8b. The peak power density of $Fe_{SA}Cu_{SA}$/NC-based MEA under the backpressure of 2.0 bar is up to 912 mW cm^{-2} (Figs. 8b and 8c), which approaches that of commercial Pt/C-based MEA (1010 mW cm^{-2}) under identical condition [55]. In addition, the peak power densities of $Fe_{SA}Cu_{SA}$/NC-based MEA decrease upon reducing the backpressure (Fig. 8b). The acidic PEMFC performance of $Fe_{SA}Cu_{SA}$/NC-based MEA also outperforms that of most Pt-free ORR catalysts reported thus far (Table S5), which is derived from its cooperative effect of highly active single atomic Fe-N_4 and Cu-N_4 sites and unique hierarchically micro/mesoporous feature [56,57].

For the purpose of exploring the realistic use of $Fe_{SA}Cu_{SA}$/NC in energy devices, a home-made Zn-air battery (ZAB) was constructed employing $Fe_{SA}Cu_{SA}$/NC covered carbon paper as the air cathode, Zn plate as the anode, as well as a mixed solution of 6 M KOH containing 0.2 M $Zn(Ac)_2$ as the electrolyte. For comparison, a benchmark ZAB assembled by applying the commercial 20 wt% Pt/C as the cathode catalyst was also evaluated. As can be observed in Fig. 8d, the ZAB based on $Fe_{SA}Cu_{SA}$/NC catalyst delivers an open-circuit voltage of as high as 1.51 V. According to the voltage-current polarization and power density plots shown in Fig. 8e, the peak power density of $Fe_{SA}Cu_{SA}$/NC-based ZAB is 127.4 mW cm^{-2}, which is much higher than that of Pt/C-based ZAB (79.8 mW cm^{-2}). In addition, the cycling stability of $Fe_{SA}Cu_{SA}$/NC-based ZAB was examined by continuous charge/discharge tests at the constant current density of 20 mA cm^{-2} (Fig. 8f). Impressively, no noticeable voltage loss can be observed after 120 charge/discharge cycles, manifesting a superior cycling durability of the $Fe_{SA}Cu_{SA}$/NC-based ZAB. Finally, as an exhibition, the $Fe_{SA}Cu_{SA}$/NC-based ZAB can continuously light up a "USTB" shaped light-emitting diode (LED) bulb for more than 12 h, demonstrating the practical utilization of $Fe_{SA}Cu_{SA}$/NC-based ZAB in powering electronic devices [58–60]. The above results indicate the great promise of $Fe_{SA}Cu_{SA}$/NC catalyst for applying in PEMFCs and ZABs.
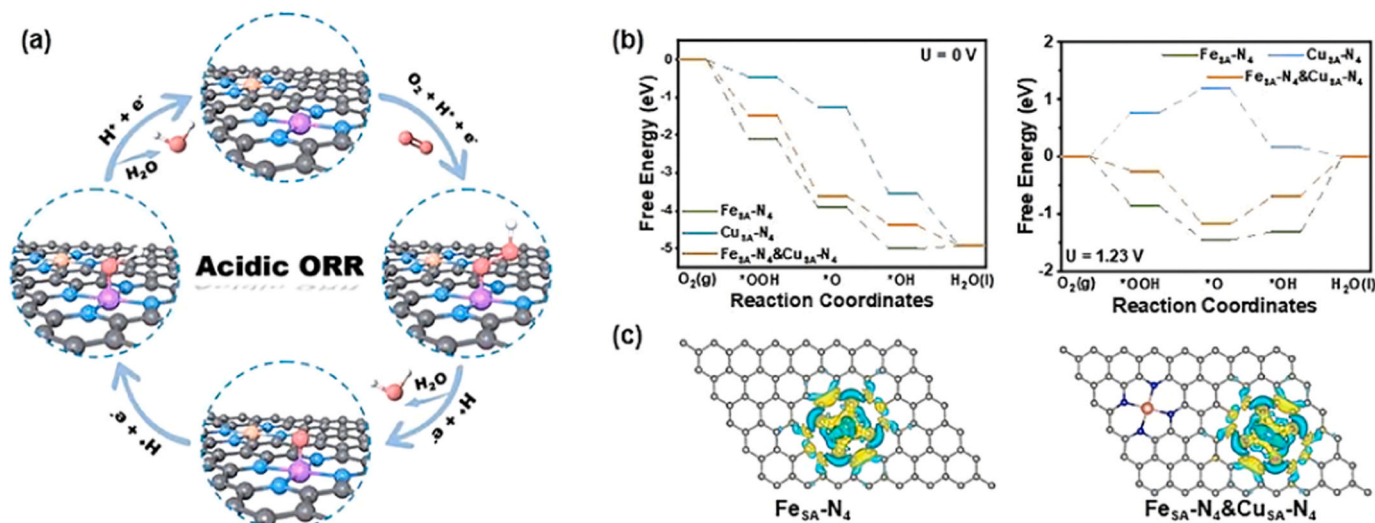
Fig. 7. (a) The proposed ORR pathway on Fe_{SA}-N_4&Cu_{SA}-N_4 model in acidic condition. (b) Calculated Gibbs free energy diagrams of ORR on Fe_{SA}/NC, Fe_{SA}/NC, and $Fe_{SA}Cu_{SA}$/NC at U = 0 V and U = 1.23 V. (c) The charge-density distribution images of Fe_{SA}-N_4 and Fe_{SA}-N_4&Cu_{SA}-N_4 models (yellow and blue areas stand for the increase and decrease in the charge density, respectively).
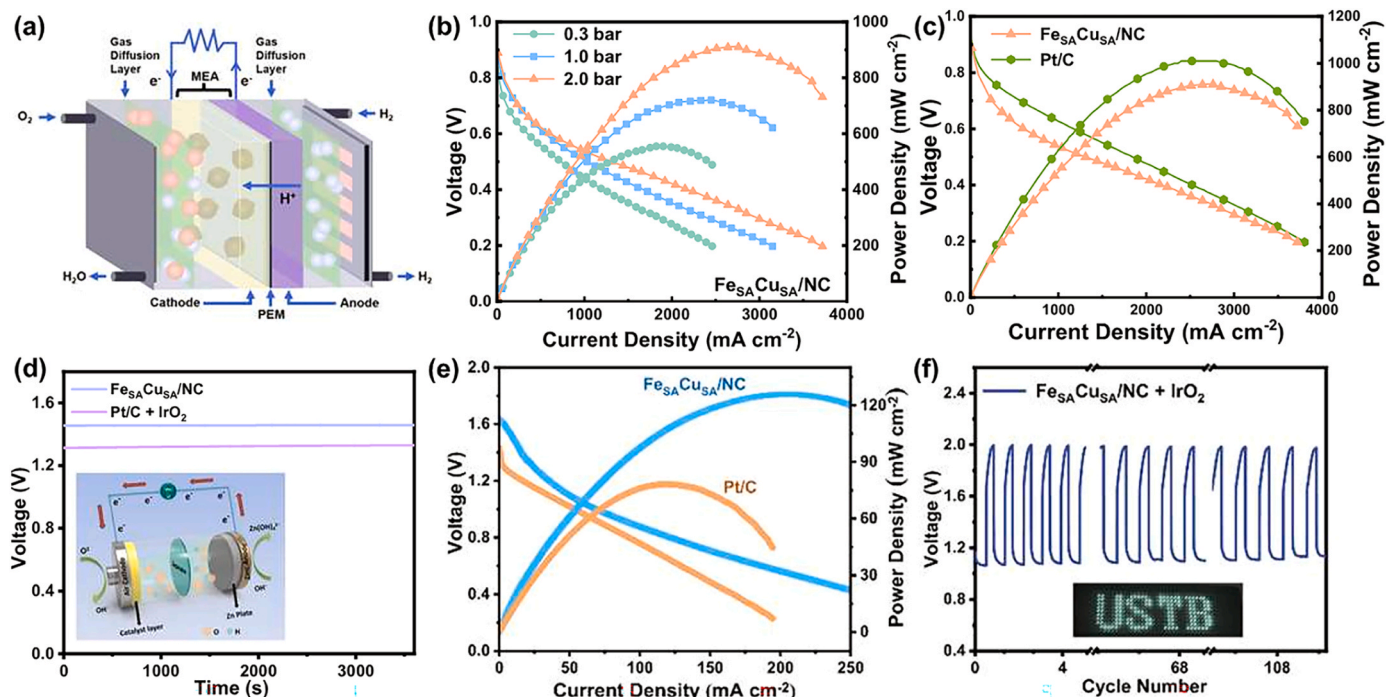
Fig. 8. (a) An illustrative diagram showing the working principle of PEMFC. (b) H_2/O_2 fuel cell polarization and power density plots of MEAs using $Fe_{SA}Cu_{SA}/NC$ as cathode catalyst under different backpressures: 0.3, 1.0, and 2.0 bar. (c) Polarization and power density curves of MEAs using $Fe_{SA}Cu_{SA}/NC$ or commercial Pt/C as the cathode catalyst under the backpressure of 2.0 bar. (d) The open circuit voltage curves of $Fe_{SA}Cu_{SA}/NC$ and Pt/C-based ZABs. Inset: an illustrative diagram showing the working principle of ZABs. (e) Polarization and corresponding power density plots of ZABs using $Fe_{SA}Cu_{SA}/NC$ and commercial Pt/C as the air electrode catalyst, respectively. (f) Charge and discharge cycling curves of the $Fe_{SA}Cu_{SA}/NC$-based ZAB at 5 mA cm^{-1}. Inset: the photograph of a LED panel powered by $Fe_{SA}Cu_{SA}/NC$-based ZAB.

4. Conclusion

In summary, we have successfully synthesized a robust asymmetric FeCu diatomic site ORR electrocatalyst containing separate single atomic Fe-N$_4$ and Cu-N$_4$ sites co-decorated on the three-dimensional porous nitrogen-doped polyhedra carbon through a feasible post-adsorption cooperative two-step pyrolysis strategy. Attributed to the advantages resulted from the cooperation of Fe atomic site and Cu atomic site as well as the highly porosity, the as-prepared catalyst possesses superior electrocatalytic performance toward ORR in both acidic and alkaline condition, featured by an $E_{1/2}$ of 0.86 V in 0.1 M HClO$_4$ and an $E_{1/2}$ of 0.88 V in 0.1 M KOH, outperforming the benchmark Pt/C, as well as splendid durability. In addition, $Fe_{SA}Cu_{SA}/NC$-based PEMFC and ZAB possess remarkable performance with preeminent power capacity. This work provides a general strategy for preparing atomically distributed dual metal site catalysts and simultaneously proposes a novel electronic configuration regulating means to boost the intrinsic activity of catalysts.

CRediT authorship contribution statement

Wang Kang: Data curation. **Wang Xinxin:** Formal analysis. **Hu Ruanbo:** Formal analysis. **Xu Qingmei:** Formal analysis. **Zheng Tianyu:** Formal analysis. **Jiang Rong:** Formal analysis. **Sun Tingting:** Conceptualization, Data curation, Writing – review & editing. **Zhang Pianpian:** Formal analysis, Investigation, Writing – original draft. **Jiang Jianzhuang:** Funding acquisition, Project administration, Supervision, Validation, Writing – review & editing. **Wang Dingsheng:** Writing – review & editing. **Xu Lianbin:** Writing – review & editing.

Declaration of Competing Interest

The authors declare that they have no known competing financial interests or personal relationships that could have appeared to influence the work reported in this paper.

Data availability

Data will be made available on request.

Appendix A. Supporting information

Supplementary data associated with this article can be found in the online version at doi:10.1016/j.apcatb.2023.123645.

References

[1] L. Shang, H. Yu, X. Huang, T. Bian, R. Shi, Y. Zhao, G.I. Waterhouse, L.Z. Wu, C.H. Tung, T. Zhang, Well-dispersed ZIF-derived Co,N-co-doped carbon nanoframes through mesoporous-silica-protected calcination as efficient oxygen reduction electrocatalysts, Adv. Mater. 28 (2016) 1668.

[2] P. Chen, T. Zhou, L. Xing, K. Xu, Y. Tong, H. Xie, L. Zhang, W. Yan, W. Chu, C. Wu, Y. Xie, Atomically dispersed iron-nitrogen species as electrocatalysts for bifunctional oxygen evolution and reduction reactions, Angew. Chem. Int. Ed. 56 (2017) 610.

[3] Z. Yang, Y. Wang, M. Zhu, Z. Li, W. Chen, W. Wei, T. Yuan, Y. Qu, Q. Xu, C. Zhao, X. Wang, P. Li, Y. Li, Y. Wu, Y. Li, Boosting oxygen reduction catalysis with Fe-N$_4$ sites decorated porous carbons toward fuel cells, ACS Catal. 9 (2019) 2158.

[4] M. Zhang, H. Li, J. Chen, F.X. Ma, L. Zhen, Z. Wen, C.Y. Xu, High-loading Co single atoms and clusters active sites toward enhanced electrocatalysis of oxygen reduction reaction for high-performance Zn-air battery, Adv. Funct. Mater. 33 (2022) 2209726.

[5] X. Luo, S. Zhao, Z. Luo, S. Li, X. Zhao, Q. Fang, X. Wei, H. Wang, C. Wang, Z. Zhu, W. Gu, Synergies of Ru/Co nanoparticles and Co single atoms active sites toward efficient electrocatalysis of oxygen reduction reaction for Zn-air battery, Chem. Eng. J. 463 (2023), 142184.

[6] W. Niu, Y. Yan, R. Li, W. Zhao, J. Chen, M. Liu, B. Gu, W. Liu, Y. Chueh, Identifying the impact of Fe nanoparticles encapsulated by nitrogen-doped carbon to Fe single atom sites for boosting oxygen reduction reaction toward Zn-air batteries, Chem. Eng. J. 456 (2023), 140858.

[7] A. Han, Z. Zhang, J. Yang, D. Wang, Y. Li, Carbon-supported single-atom catalysts for formic acid oxidation and oxygen reduction reactions, Small 17 (2021) 2004500.

[8] X. Shu, Q. Chen, M. Yang, M. Liu, J. Ma, J. Zhang, Tuning Co-catalytic sites in hierarchical porous N-doped carbon for high-performance rechargeable and flexible Zn-air battery, Adv. Energy Mater. 13 (2023) 2202871.

[9] J. Yan, X. Zheng, C. Wei, Z. Sun, K. Zeng, L. Shen, J. Sun, M.H. Rümmeli, R. Yang, Nitrogen-doped hollow carbon polyhedron derived from salt-encapsulated ZIF-8 for efficient oxygen reduction reaction, Carbon 171 (2021) 320.

[10] Y. Zhang, J. Li, Q. Peng, P. Yang, Q. Fu, X. Zhu, Q. Liao, Toward an objective performance evaluation of commercial Pt/C electrocatalysts for oxygen reduction: effect of catalyst loading, Electrochim. Acta 429 (2022), 140953.

[11] S. Fu, C. Zhu, J. Song, M.H. Engelhard, H. Xia, D. Du, Y. Lin, Kinetically controlled synthesis of Pt-based one-dimensional hierarchically porous nanostructures with large mesopores as highly efficient ORR catalysts, ACS Appl. Mater. Interfaces 8 (2016) 35213.

[12] J. Wang, Z. Huang, W. Liu, C. Chang, H. Tang, Z. Li, W. Chen, C. Jia, T. Yao, S. Wei, Y. Wu, Y. Li, Design of N-coordinated dual-metal sites: a stable and active Pt-free catalyst for acidic oxygen reduction reaction, J. Am. Chem. Soc. 139 (2017) 17281.

[13] R. Adhikary, D. Sarkar, M. Mukherjee, J. Datta, Remarkable performance of the unique Pd–Fe2O3 catalyst towards OER and ORR: non-Pt and non-carbon electrode materials for low-temperature fuel cells, J. Mater. Chem. A 9 (2021) 3052.

[14] S. Polani, K. MacArthur, J. Kang, M. Klingenhof, X. Wang, T. Moller, R. Amitrano, R. Chattot, M. Heggen, R. Dunin-Borkowski, P. Strasser, Highly active and stable large Mo-doped Pt-Ni octahedral catalysts for ORR: synthesis, post-treatments, and electrochemical performance and stability, ACS Appl. Mater. Interfaces 14 (2022) 29690.

[15] L. Peng, L. Shang, T. Zhang, G. Waterhouse, Recent advances in the development of single-atom catalysts for oxygen electrocatalysis and zinc-air batteries, Adv. Energy Mater. 10 (2020) 2003018.

[16] Y. Wang, X. Zheng, D. Wang, Design concept for electrocatalysts, Nano Res. 15 (2022) 1730–1752.

[17] T. Cui, Y. Wang, T. Ye, J. Wu, Z. Chen, J. Li, Y. Lei, D. Wang, Y. Li, Engineering dual single-atom sites on 2D ultrathin N-doped carbon nanosheets attaining ultra-low-temperature zinc-air battery, Angew. Chem. Int. Ed. 61 (2022), e202115219.

[18] C. Chen, Z. Tang, J. Li, C. Du, T. Ouyang, K. Xiao, Z. Liu, MnO enabling highly efficient and stable Co-Nx/C for oxygen reduction reaction in both acidic and alkaline media, Adv. Funct. Mater. 33 (2023) 2210143.

[19] J. Chen, B. Huang, R. Cao, L. Li, X. Tang, B. Wu, Y. Wu, T. Hu, K. Yuan, Y. Chen, Steering local electronic configuration of Fe-N-C-based coupling catalysts via ligand engineering for efficient oxygen electroreduction, Adv. Funct. Mater. 33 (2023) 2209315.

[20] H. Li, K. Gan, R. Li, H. Huang, J. Niu, Z. Chen, J. Zhou, Y. Yu, J. Qiu, X. He, Highly dispersed NiO clusters induced electron delocalization of Ni-N-C catalysts for enhanced CO₂ electroreduction, Adv. Funct. Mater. 33 (2023) 2208622.

[21] H. Liu, L. Jiang, J. Khan, X. Wang, J. Xiao, H. Zhang, H. Xie, L. Li, S. Wang, L. Han, Decorating single-atomic Mn sites with FeMn clusters to boost oxygen reduction reaction, Angew. Chem. Int. Ed. 62 (2023), e202214988.

[22] X. Wang, Y. Jin, R. Jiang, H. Wang, Z. Gao, P. Zhang, X. Liu, X. Xiao, D. Qi, T. Wang, J. Jiang, Cobalt nanocluster-decorated N-rich hierarchical carbon architectures efficiently catalyze oxygen reduction and hydrogen evolution reactions, ACS Sustain. Chem. Eng. 10 (2022) 2001.

[23] R. Jiang, X. Chen, J. Deng, T. Wang, K. Wang, Y. Chen, J. Jiang, In-situ growth of ZnS/FeS heterojunctions on biomass-derived porous carbon for efficient oxygen reduction reaction, J. Energy Chem. 47 (2020) 79.

[24] Z. Gao, P. Zhang, R. Jiang, H. Wang, Q. Zhi, B. Yu, Y. Jin, T. Sun, J. Jiang, Co-Fe alloy nanoparticles and Fe₃C nanocrystals on N-doped biomass-derived porous carbon for superior electrocatalytic oxygen reduction, J. Solid State Chem. 307 (2022) 122735.

[25] X. Xie, L. Peng, H. Yang, G. Waterhouse, L. Shang, T. Zhang, MIL-101-derived mesoporous carbon supporting highly exposed Fe single-atom sites as efficient oxygen reduction reaction catalysts, Adv. Mater. 33 (2021) 2101038.

[26] S. Hong, K. Ham, J. Hwang, S. Kang, M.H. Seo, Y.W. Choi, B. Han, J. Lee, K. Cho, Active motif change of Ni-Fe spinel oxide by Ir doping for highly durable and facile oxygen evolution reaction, Adv. Funct. Mater. 33 (2023) 2209543.

[27] J. Chen, H. Li, C. Fan, Q. Meng, Y. Tang, X. Qiu, G. Fu, T. Ma, Dual single-atomic Ni-N(4) and Fe-N(4) sites constructing janus hollow graphene for selective oxygen electrocatalysis, Adv. Mater. 32 (2020) 2003134.

[28] Y. He, X. Yang, Y. Li, L. Liu, S. Guo, C. Shu, F. Liu, Y. Liu, Q. Tan, G. Wu, Atomically dispersed Fe-Co dual metal sites as bifunctional oxygen electrocatalysts for rechargeable and flexible Zn-air batteries, ACS Catal. 12 (2022) 1216.

[29] X. Zheng, B. Li, Q. Wang, D. Wang, Y. Li, Emerging low-nuclearity supported metal catalysts with atomic level precision for efficient heterogeneous catalysis, Nano Res. 15 (2022) 7806–7839.

[30] R. Li, D. Wang, Understanding the structure-performance relationship of active sites at atomic scale, Nano Res. 15 (2022) 6888–6923.

[31] W. Li, J. Yang, D. Wang, Long-range interactions in diatomic catalysts boosting electrocatalysis, Angew. Chem. Int. Ed. 61 (2022), e202213318.

[32] A. Bhagi-Damodaran, M. Michael, Q. Zhu, J. Reed, B. Sandoval, E. Mirts, S. Chakraborty, P. Moenne-Loccoz, Y. Zhang, Y. Lu, Why copper is preferred over iron for oxygen activation and reduction in Haem-Copper oxidases, Nat. Chem. 9 (2017) 257.

[33] S. Kim, B. Seo, H. Jeong, J. Shim, Atomic layer deposited Pt/Cu bimetallic catalysts for use in high-performance fuel cell cathodes, Int. J. Energy Res. 46 (2022) 17180.

[34] H. Zhang, Q. Sun, Q. He, Y. Zhang, X. He, T. Gan, H. Ji, Single Cu atom dispersed on S,N-codoped nanocarbon derived from shrimp shells for highly-efficient oxygen reduction reaction, Nano Res. 15 (2022) 5995.

[35] Y. Qu, Z. Li, W. Chen, Y. Lin, T. Yuan, Z. Yang, C. Zhao, J. Wang, C. Zhao, X. Wang, F. Zhou, Z. Zhuang, Y. Wu, Y. Li, Direct transformation of bulk copper into copper single sites via emitting and trapping of atoms, Nat. Catal. 1 (2018) 781.

[36] S. Lee, J. Kim, D. Chung, J. Yoo, H. Lee, M. Kim, B. Mun, S. Kwon, Y. Sung, T. Hyeon, Design principle of Fe-N-C electrocatalysts: how to optimize multimodal porous structures? J. Am. Chem. Soc. 141 (2019) 2035.

[37] Y. Li, H. Zhang, Y. Wang, P. Liu, H. Yang, X. Yao, D. Wang, Z. Tang, H. Zhao, A self-sponsored doping approach for controllable synthesis of S and N co-doped trimodal-porous structured graphitic carbon electrocatalysts, Energy Environ. Sci. 7 (2014) 3720.

[38] X. Hu, Y. Liu, W. Cui, X. Yang, J. Li, S. Zheng, B. Yang, Z. Li, X. Sang, Y. Li, L. Lei, Y. Hou, Boosting industrial-level CO₂ electroreduction of N-doped carbon nanofibers with confined tin-nitrogen active sites via accelerating proton transport kinetics, Adv. Funct. Mater. 33 (2023) 2208781.

[39] Y. Wang, J. Wu, S. Tang, J. Yang, C. Ye, J. Chen, Y. Lei, D. Wang, Synergistic Fe-Se atom pairs as bifunctional oxygen electrocatalysts boost low-temperature rechargeable Zn-air battery, Angew. Chem. Int. Ed. 62 (2023), e202219191.

[40] S. Lee, J. Kim, D. Chung, J. Yoo, H. Lee, M. Kim, B. Mun, S. Kwon, Y. Sung, T. Hyeon, Design principle of Fe-N-C electrocatalysts: how to optimize multimodal porous structures? J. Am. Chem. Soc. 141 (2019) 2035.

[41] M. Chen, M. Zhu, M. Zuo, S. Chu, J. Zhang, Y. Wu, H. Liang, X. Feng, Identification of catalytic sites for oxygen reduction in metal/nitrogen-doped carbons with encapsulated metal nanoparticles, Angew. Chem. Int. Ed. 59 (2020) 1627.

[42] T. Zhou, Y. Du, S. Yin, X. Tian, H. Yang, X. Wang, B. Liu, H. Zheng, S. Qiao, R. Xu, Nitrogen-doped cobalt phosphate@nanocarbon hybrids for efficient electrocatalytic oxygen reduction, Energy Environ. Sci. 9 (2016) 2563.

[43] W. Zhong, Y. Qiu, H. Shen, X. Wang, J. Yuan, C. Jia, S. Bi, J. Jiang, Electronic spin moment as a catalytic descriptor for Fe single-atom catalysts supported on C₂N, J. Am. Chem. Soc. 143 (2021) 4405.

[44] H. Shang, X. Zhou, J. Dong, A. Li, X. Zhao, Q. Liu, Y. Lin, J. Pei, Z. Li, Z. Jiang, D. Zhou, L. Zheng, Y. Wang, J. Zhou, Z. Yang, R. Cao, R. Sarangi, T. Sun, X. Yang, X. Zheng, W. Yan, Z. Zhuang, J. Li, W. Chen, D. Wang, J. Zhang, Y. Li, Engineering unsymmetrically coordinated Cu-S₁N₃ single atom sites with enhanced oxygen reduction activity, Nat. Commun. 11 (2020) 3049.

[45] A. Han, X. Wang, K. Tang, Z. Zhang, C. Ye, K. Kong, H. Hu, L. Zheng, P. Jiang, C. Zhao, Q. Zhang, D. Wang, Y. Li, An adjacent atomic platinum site enables single-atom iron with high oxygen reduction reaction performance, Angew. Chem. Int. Ed. 60 (2021) 19262.

[46] T. Sun, S. Zhao, W. Chen, D. Zhai, J. Dong, Y. Wang, S. Zhang, A. Han, L. Gu, R. Yu, X. Wen, H. Ren, L. Xu, C. Chen, Q. Peng, D. Wang, Y. Li, Single-atomic cobalt sites embedded in hierarchically ordered porous nitrogen-doped carbon as a superior bifunctional electrocatalyst, Proc. Natl. Acad. Sci. USA 11 (2018) 12692.

[47] M. Xiao, L. Gao, Y. Wang, X. Wang, J. Zhu, Z. Jin, C. Liu, H. Chen, G. Li, J. Ge, Q. He, Z. Wu, Z. Chen, W. Xing, Engineering energy level of metal center: Ru single-atom site for efficient and durable oxygen reduction catalysis, J. Am. Chem. Soc. 141 (2019) 19800.

[48] Z. Wang, H. Jin, T. Meng, K. Liao, W. Meng, J. Yang, D. He, Y. Xiong, S. Mu, Fe, Cu-coordinated ZIF-derived carbon framework for efficient oxygen reduction reaction and zinc-air batteries, Adv. Funct. Mater. 28 (2018) 1802596.

[49] F. Xiao, Q. Wang, G. Xu, X. Qin, I. Hwang, C. Sun, M. Liu, W. Hua, H. Wu, S. Zhu, J. Li, J. Wang, Y. Zhu, D. Wu, Z. Wei, M. Gu, K. Amine, M. Shao, Atomically dispersed Pt and Fe sites and Pt-Fe nanoparticles for durable proton exchange membrane fuel cells, Nat. Catal. 5 (2022) 503.

[50] Y. Zhang, S. Zhang, H. Huang, X. Liu, B. Li, Y. Lee, X. Wang, Y. Bai, M. Sun, Y. Wu, S. Gong, X. Liu, Z. Zhuang, T. Tan, Z. Niu, General synthesis of a diatomic catalyst library via a macrocyclic precursor-mediated approach, J. Am. Chem. Soc. 145 (2023) 4819.

[51] C. Du, Y. Gao, H. Chen, P. Li, S. Zhu, J. Wang, Q. He, W. Chen, A Cu and Fe dual-atom nanozyme mimicking cytochrome c oxidase to boost the oxygen reduction reaction, J. Mater. Chem. A 8 (2020) 16994.

[52] M. Wang, P. Gao, D. Li, X. Wu, M. Yang, Z. Li, Y. Shen, X. Hu, Y. Liu, Z. Chen, Cu/Fe dual atoms catalysts derived from Cu-MOF for Zn-air batteries, Mater. Today Energy 28 (2022), 101086.

[53] J. Li, W. Xia, J. Tang, Y. Gao, C. Jiang, Y. Jia, T. Chen, Z. Hou, R. Qi, D. Jiang, T. Asahi, X. Xu, T. Wang, J. He, Y. Yamauchi, Metal-organic framework-derived graphene mesh: a robust scaffold for highly exposed Fe-N₄ active sites toward an excellent oxygen reduction catalyst in acid media, J. Am. Chem. Soc. 144 (2022) 9280.

[54] S. Liu, C. Li, M. Zachman, Y. Zeng, H. Yu, B. Li, M. Wang, J. Braaten, J. Liu, H. Meyer, M. Lucero, A. Kropf, E. Alp, Q. Gong, Q. Shi, Z. Feng, H. Xu, G. Wang, D. Myers, J. Xie, D. Cullen, S. Litster, G. Wu, Atomically dispersed iron sites with a nitrogen-carbon coating as highly active and durable oxygen reduction catalysts for fuel cells, Nat. Energy 7 (2022) 652.

[55] M. Qiao, Y. Wang, Q. Wang, G. Hu, X. Mamat, S. Zhang, S. Wang, Hierarchically ordered porous carbon with atomically dispersed FeN4 for ultraefficient oxygen reduction reaction in proton-exchange membrane fuel cells, Angew. Chem. Int. Ed. 59 (2020) 2688.

[56] Y. Chen, S. Ji, S. Zhao, W. Chen, J. Dong, W. Cheong, R. Shen, X. Wen, L. Zheng, A. Rykov, S. Cai, H. Tang, Z. Zhuang, C. Chen, Q. Peng, D. Wang, Y. Li, Enhanced oxygen reduction with single-atomic-site iron catalysts for a zinc-air battery and hydrogen-air fuel cell, Nat. Commun. 9 (2018) 5422.

[57] L. Guo, S. Hwang, B. Li, F. Yang, M. Wang, M. Chen, X. Yang, G.S. Karakalos, A. D. Cullen, Z. Feng, G. Wang, G. Wu, H. Xu, Promoting atomically dispersed MnN_4 sites via sulfur doping for oxygen reduction: unveiling intrinsic activity and degradation in fuel cells, ACS Nano 15 (2021) 6886.

[58] G. Chen, P. Liu, Z. Liao, F. Sun, Y. He, H. Zhong, T. Zhang, E. Zschech, M. Chen, G. Wu, J. Zhang, X. Feng, Zinc-mediated template synthesis of Fe-N-C electrocatalysts with densely accessible Fe-Nx active sites for efficient oxygen reduction, Adv. Mater. 32 (2020) 1907399.

[59] M. Jiao, Q. Zhang, C. Ye, R. Gao, L. Dai, G. Zhou, H. Cheng, Isolating contiguous Fe atoms by forming a Co-Fe intermetallic catalyst from spent lithium-ion batteries to regulate activity for zinc-air batteries, ACS Nano 16 (2022) 13223.

[60] M. Xiao, Z. Xing, Z. Jin, C. Liu, J. Ge, J. Zhu, Y. Wang, X. Zhao, Z. Chen, Preferentially engineering FeN_4 edge sites onto graphitic nanosheets for highly active and durable oxygen electrocatalysis in rechargeable Zn-air batteries, Adv. Mater. 32 (2020) 2004900.